Check for updates

A flow-circulation system incorporating a PVP-BiOBr@rGO assembly for simultaneous degradation and detection of oxytetracycline in fish farm wastewater†

Saowapak Teerasong, [ID] *[ab] Nichakarn Suknakhin,[b] Thanamat Sonsaket,[b] Wanatchaporn Teerasong,[c] Chesta Ruttanapun,[d] Chaval Sriwong,[e] Apiwat Chompoosor[f] and Suwat Nanan [ID] [g]

This work focuses on developing a new flow-circulation system for simultaneous detection and degradation of oxytetracycline (OTC) in fish farm wastewater to address a need for antibiotic abatement in wastewater treatment. Polyvinyl pyrrolidone capped bismuth oxybromide assembled with a reduced graphene oxide (PVP-BiOBr@rGO) photocatalyst was solvothermally synthesized and characterized. The prepared photocatalyst exhibited a morphological flower-like structure with a high surface area, 47.59 $m^2 g^{-1}$. Its band gap energy was 2.93 eV. A ternary PVP-BiOBr@rGO composite showed lower charge recombination than its pure form. PVP-BiOBr@rGO was filled inside a catalyst column of a flow system, with a spectrophotometer at the column end. Wastewater was continuously transported through the column and OTC spectrophotometrically examined during its degradation. The wastewater was recirculated until the OTC concentration was minimized. This system achieved 90.3% degradation of OTC within 180 min. The catalyst column could be regenerated for 2 cycles. The proposed flow system offers the advantages of ease of use, inline operation, and real-time sensing. This highlights a potential for real-world sustainable wastewater treatment applications.

1. Introduction

Antibiotics are often used in animal agriculture (*e.g.*, poultry and fish farms) to treat diseases and promote growth. There is some information on antibiotic use in animal agriculture. It is estimated that approximately 80% of all antibiotics sold in the

[a]Flow Innovation-Research for Science and Technology Laboratories (FIRST Labs), Thailand. E-mail: saowapak.te@kmitl.ac.th

[b]Department of Chemistry and Applied Analytical Chemistry Research Unit, School of Science, King Mongkut's Institute of Technology Ladkrabang, Bangkok 10520, Thailand

[c]Department of Chemical Engineering, King Mongkut's University of Technology Thonburi, Bangkok 10140, Thailand

[d]Department of Physics and Smart Materials Research and Innovation Unit, School of Science, King Mongkut's Institute of Technology Ladkrabang, Bangkok 10520, Thailand

[e]Department of Chemistry and Smart Materials Research and Innovation Unit, School of Science, King Mongkut's Institute of Technology Ladkrabang, Bangkok 10520, Thailand

[f]Department of Chemistry and Center of Excellence for Innovation in Chemistry, Faculty of Science, Ramkhamhaeng University, Bangkok 10240, Thailand

[g]Materials Chemistry Research Center, Department of Chemistry and Center of Excellence for Innovation in Chemistry, Faculty of Science, Khon Kaen University, Khon Kaen 40002, Thailand

† Electronic supplementary information (ESI) available. See DOI: https://doi.org/10.1039/d5ra01825k

U.S. are administered for animal farming.[1] Antibiotic use on farms is anticipated to grow by 8% between 2020 and 2030.[2] There are global concerns about their excessive use. Amongst the various antibiotics, oxytetracycline (OTC), a broad-spectrum drug widely used in medicine and agriculture,[3] has been identified as a prominent wastewater contaminant. Due to its hydrophilic nature and low volatility, OTC residues can persist in soil, natural water and even drinking water. OTC contamination in the environment contributes to the development of antibiotic-resistant microorganisms,[4] which harm humans by increasing the risk of certain infections. Therefore, OTC residue removal is needed before discharging farm wastewater into the environment.

Physicochemical methods such as membrane filtration and adsorption processes have been adopted for OTC removal.[5,6] However, the major drawback of such processes is that they only transfer the drug from one phase to another, leaving it in a toxic form. Advanced photochemical processes are interesting ways to solve environmental problems. These methods involve clean and sustainable treatments, which use light radiation to convert pollutants into innocuous forms. Numerous photocatalytic materials have been proposed for the degradation of OTC, for example, ZnO, g-C_3N_4, ZnO/NiO, CuO/Bi_2WO_6, and benzene polymer/Bi_2MoO_6/GO, among others.[7–11] Heterostructure

photocatalysts have attracted increasing attention compared to single-component systems. By combining different materials, these composites can optimize light harvesting, facilitate efficient charge carrier separation, and enhance redox capabilities, resulting in significantly improved photocatalytic activity.[12,13]

Bismuth oxybromide (BiOBr) photocatalysts have gained consideration for their unique properties which include visible-light absorption, facile synthesis, low toxicity, and high photocatalytic efficiency. Their efficiency can be further improved through several modifications, *viz.*, metal/non-metal doping, heterojunction construction, and carbon-based hybrid composites.[14,15] Polyvinyl pyrrolidone (PVP) was employed as a capping agent to control the structural, morphological, and surface properties of BiOBr, and thus the photocatalytic activity of PVP-BiOBr for degrading pollutants. It was enhanced compared to an unmodified BiOBr photocatalyst.[16–18] Reduced graphene oxide (rGO), with its ultrahigh surface area and excellent electrical properties, has been established for use in a hybrid with BiOBr photocatalyst.[19–21] rGO acts as an electron acceptor, which enables photogenerated electron transfer and extends the lifespan of electron–hole pair recombination, hence photocatalytic activity is significantly enhanced.[22,23] Additionally, the adsorption capability of rGO, hybrid composites offer a synergistic effect, combining both adsorption and photocatalysis for more effective pollutant removal.[24,25]

Much recent research has proposed various photocatalysts for pollutant removal from wastewater. However, these studies used batch conditions.[8–11,16–20,23–25] Conventional batch methods have inherent drawbacks in real-world applications. After photocatalytic treatment, it is difficult to separate the photocatalysts from the treated water and regenerate them.[26] To overcome this limitation, innovative flow-based methods have emerged as promising alternatives. Recently, continuous flow-circulation systems have been developed for photocatalytic and adsorptive removal of ammonia, phenols, and indigo carmine dye.[27,28] A pollutant-containing solution was fed from a sample vessel to a catalyst reactor by a peristaltic pump. The effluent was returned to the sample vessel and transferred to the reactor again until the pollutant concentration was sufficiently reduced. With a flow-circulation system, catalysts were trapped in a reactor and were not suspended in the treated water. Consequently, it is easier to regenerate and reuse catalysts in practical water treatment applications.

In this study, we developed an innovative flow-based system that integrates a PVP-BiOBr@rGO photocatalyst to enable inline degradation and real-time detection of oxytetracycline (OTC). A PVP-BiOBr@rGO photocatalyst was synthesized using a facile solvothermal method, followed by comprehensive characterization to reveal its morphological, structural, and optical properties. We stored the photocatalyst in a flow-through column connected to a downstream spectrophotometer. As the influent passed through the column and detector, OTC was effectively degraded, with residual levels promptly measured. We also evaluated the reusability of the synthesized catalyst. The developed system demonstrated its usefulness in treating OTC-contaminated wastewater from fish farms, showing its potential for practical applications in environmental remediation of OTC contamination.

2. Experimental

2.1. Synthesis of PVP-BiOBr

PVP-BiOBr was synthesized *via* a solvothermal method according to our previous report.[16] In a typical procedure, 0.075 M bismuth nitrate pentahydrate was prepared by weighing 1.0907 g of $Bi(NO_3)_3 \cdot 5H_2O$ (Sigma-Aldrich, USA) into 30 mL of ethylene glycol (Sigma-Aldrich, USA) with vigorous stirring for 30 min. Then, 0.3010 g of polyvinyl pyrrolidone (MW 40 000) (Sigma-Aldrich, USA) was incorporated into the bismuth nitrate solution. Separately, a 0.071 M potassium bromide solution was prepared by dissolving 0.2546 g of KBr (Ajax Finechem, Australia) in 30 mL of ethylene glycol under vigorous stirring for 30 min. The potassium bromide solution was added to the bismuth nitrate solution with subsequent stirring for 1 h. After that, the mixture was transferred to a Teflon-lined stainless steel autoclave and heated at 160 °C for 12 h. A gray precipitate was obtained. The precipitate was collected by filtration and washed with DI water and ethanol at least 3 times. Finally, the product was dried at 60 °C for 6 h. For comparison, the bare BiOBr photocatalyst was synthesized using the procedure described above with no PVP addition.

2.2. Synthesis of rGO

Reduced graphene oxide (rGO) was prepared from chemically or thermally treated graphene oxide (GO), as previously reported.[29] Briefly, 100 mL of a GO suspension ($2~mg~mL^{-1}$) was mixed with 100 mL of DI water, 1 mL of a 30% ammonia solution (Baker, USA), and 0.1 mL of a 65% hydrazine hydrate solution (Sigma-Aldrich, USA). The mixture was heated and stirred at 95 °C in an oil bath for 45 min. An rGO suspension was obtained. The rGO powder was collected by vacuum filtration and dried overnight at 60 °C. A general procedure for synthesis of the starting GO is provided in the Supplementary Information.†

2.3. Synthesis of PVP-BiOBr@rGO composite

The PVP-BiOBr@rGO composite was prepared based on previous work with some modifications.[19] Typically, 20 mg of rGO was dispersed in 30 mL of an ethanol : water solution (2 : 1 v/v) with ultrasonication for 1 h. Subsequently, 100 mg of PVP-BiOBr was added to the rGO suspension. The mixed solution was further sonicated for 1 h. After that, the suspension was maintained at 120 °C for 3 h in a Teflon-lined stainless-steel autoclave. The resulting composite was filtered, washed with DI water and ethanol, and dried at 60 °C. The PVP-BiOBr@rGO composite was kept in a desiccator until further use.

2.4. Characterizations

The synthesized composite was characterized using various techniques. Morphology was examined using scanning electron microscopy (SEM, SU8000 Hitachi), operating at 10 kV. Chemical composition was assessed using energy dispersive X-ray spectroscopy (EDX) as part of the SEM apparatus. PVP-

BiOBr@rGO crystal structure and purity were determined using X-ray diffraction (XRD, Smartlab Rigaku) with Cu-Kα radiation ($\lambda = 1.5406$ Å) and a 2θ scan range of 5–80°. Specific surface area was measured using N_2 adsorption–desorption isotherms at 77.3 K, applying the Brunauer–Emmett–Teller (BET) equation. Pore size distribution was determined using desorption isotherms and the Barret–Joyner–Halenda (BJH) method (Micromeritics 3Flex). Diffuse reflectance spectra were studied using UV-vis spectrophotometry (UV-2600 Shimadzu). Photoluminescence spectra were recorded with a spectrofluorometer (RF-5301PC Shimadzu) at an excitation wavelength (λ_{ex}) of 250 nm.

2.5. Batch study

Batch experiments were performed to find optimal conditions for photocatalytic degradation of OTC by the PVP-BiOBr@rGO photocatalyst. Ten mg of photocatalyst was suspended in 40 mL of a 10 mg L^{-1} OTC standard solution. The suspension was stirred in the dark for 60 min to obtain an adsorption–desorption equilibrium before light irradiation. At 15-min intervals, 3 mL of an OTC solution was sampled, centrifuged, and transferred into a cuvette for spectrophotometric absorbance measurements at 368 nm. Then, the concentration of OTC was analyzed.

2.6. Flow-circulation set-up

A flow-circulation system was constructed as shown in Fig. 1. The photocatalyst column was fabricated using transparent Tygon tubing (2 cm long) and two nylon syringe filters (0.45 μm, Millipore, USA) attached to the ends, packed with 10 mg of PVP-BiOBr@rGO. The column was placed under two fluorescent lamps (24 Watts, Philips, UK). Forty mL of wastewater containing OTC was transported from a sample container through the flow system using a peristaltic pump (ISM827B Ismatec, USA) at 1.0 mL min^{-1}. A spectrophotometer coupled with a flow-through cell (10 mm path length, Hellma Analytics, UK) was located after the photocatalyst column to monitor the OTC absorbance at 368 nm. The wastewater sample was returned to
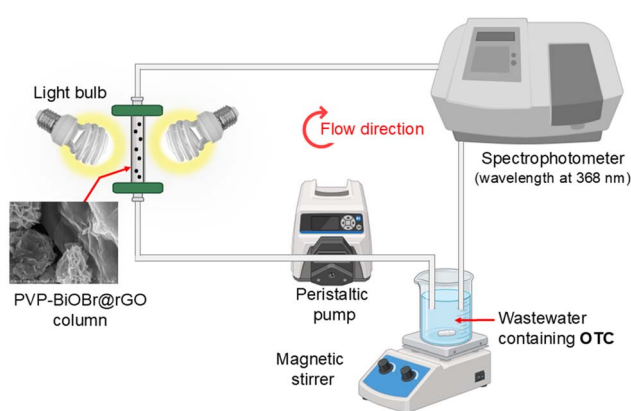

Fig. 1 Schematic of a flow-circulation system with a PVP–BiOBr@rGO photocatalyst incorporated for in-line removal and monitoring of oxytetracycline.
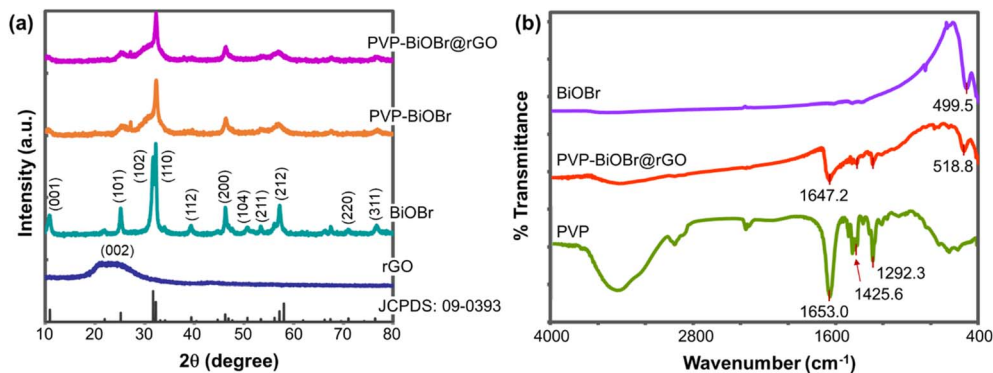
a container and re-circulated into the system until the %photodegradation reached 90%. The sample solution was continuously stirred in this container to supply dissolved oxygen for the photocatalytic reaction.

Wastewater samples were collected from carp fish farm effluents (Lop Buri, Thailand). The samples were filtered through a 0.45 μm membrane filter to remove particulate matter and spiked with 10 mg L^{-1} of a standard OTC solution, before transfer into the flow system. OTC concentration in the sample solution was analyzed as a function of time. Photodegradation efficiency was determined using eqn (1):

$$\% \text{ Photodegradation} = \left(\frac{C_0 - C_t}{C_0}\right) \times 100 \quad (1)$$

where C_0 is the initial concentration and C_t is the concentration at time t of OTC (mg L^{-1}) in the sample solutions, respectively.

3. Results and discussion

3.1. PVP-BiOBr@rGO characteristics

The XRD patterns of BiOBr, PVP-BiOBr, PVP-BiOBr@rGO, and rGO are shown in Fig. 2a. The main characteristic peaks of these materials match the standard pattern of the tetragonal-structured BiOBr (JCPDS No. 09-0393), demonstrating formation of BiOBr in the composite.[16] Diffraction peaks at 25.2°, 32.2°, 46.3°, 57.1°, 67.5°, and 76.7° were ascribed to the (101), (110), (200), (212), (220) and (311) planes, respectively.[20] However, the intensity of those peaks in PVP-BiOBr and PVP-BiOBr@rGO was weaker than those of pure BiOBr. Crystallite sizes were calculated by applying the Debye–Scherrer equation for distinct peaks ($2\theta = 25.2°$, 46.3°, and 57.1°). The average crystallite sizes of BiOBr, PVP-BiOBr and PVP-BiOBr@rGO were 12.4, 8.72 and 8.68 nm, respectively. With PVP addition, PVP was coordinated on the surface of BiOBr and reduced the crystallite size.[17] The standard pattern of rGO, according to JCPDS No. 75-2078, exhibits a prominent peak at 26° corresponding to the (002) plane.[30] However in this work, rGO contributes insignificantly to the crystallinity of the composite. A diffraction peak of rGO was not observed, perhaps due to its relatively low content in the composite or increasingly disordered stacking of rGO, rendering them undetectable by XRD.[31]

FTIR spectroscopy was conducted to examine the functional groups in the synthesized composites. As shown in Fig. 2b, the FTIR spectrum of pure PVP displays a distinctive C=O stretching band at 1653.0 cm^{-1}, associated with the pyrrolidone group.[18] Additional characteristic bands of PVP include C-N stretching at 1292.3 cm^{-1} and –CH$_2$ absorption at 1425.6 cm^{-1}.[32] In contrast, the spectrum of bare BiOBr shows a prominent band at 499.5 cm^{-1}, attributed to the symmetric stretching vibration of the Bi–O bond.[33] Upon incorporating PVP into BiOBr, the C=O stretching band shifts from 1653.0 cm^{-1} to 1647.2 cm^{-1} in the composite, confirming successful inclusion of PVP. This slight red shift indicates a physical adsorption mechanism rather than covalent bonding.[18,32]

Raman spectroscopy was performed to verify the presence of rGO in the PVP-BiOBr@rGO composite. In Fig. S1,† rGO

Fig. 2 (a) XRD patterns of BiOBr, PVP-BiOBr, PVP-BiOBr@rGO, rGO and standard BiOBr (JCPDS No. 09-0393), and (b) FTIR spectra of pure PVP, BiOBr and PVP-BiOBr@rGO.

displays two main peaks at about 1346 and 1583 cm^{-1}, which correspond to disordered sp^2 carbon (D-band) and well-ordered graphite (G-band), respectively.[23] These two typical peaks were also observed in the Raman spectrum of the PVP-BiOBr@rGO, demonstrating successful integration of rGO into the ternary composite structure. Additionally, the D to G intensity ratio for the composite is greater than 1, suggesting primarily a reduced form of graphene oxide.[29]

The morphology of BiOBr, PVP-BiOBr and PVP-BiOBr@rGO composites were characterized using SEM. In Fig. 3a and b, BiOBr and PVP-BiOBr illustrate similar spherical microstructures formed by numerous self-assembled petal-like nanosheets. The size of the PVP-BiOBr was ∼1 μm, which was smaller than that of bare BiOBr, ∼2 μm. The particle size evaluated from

SEM micrographs is consistent with the crystallite size calculated from XRD. Remarkably, PVP-BiOBr is comprised of more microporous features than the bare BiOBr. A SEM image of PVP-BiOBr@rGO is shown in Fig. 3c. Petal-like PVP-BiOBr microspheres are observed, with the presence of rGO nanoplates. PVP-BiOBr and rGO are closely attached, which confirms that a hybrid composite with interfacial conjunction was successfully prepared. This could assist charge transfer during photoreactions.[24] EDX analysis of the ternary composite indicated the presence of Bi, Br, O and C atoms in the composite (Fig. 3d). The Bi to Br atomic ratio in both pure BiOBr and the PVP-BiOBr@rGO composite is close to 1 : 1, consistent with its expected stoichiometry. In pure BiOBr, the oxygen content also reflects its 1 : 1 : 1 Bi : O : Br composition (Fig. S2†). In contrast,
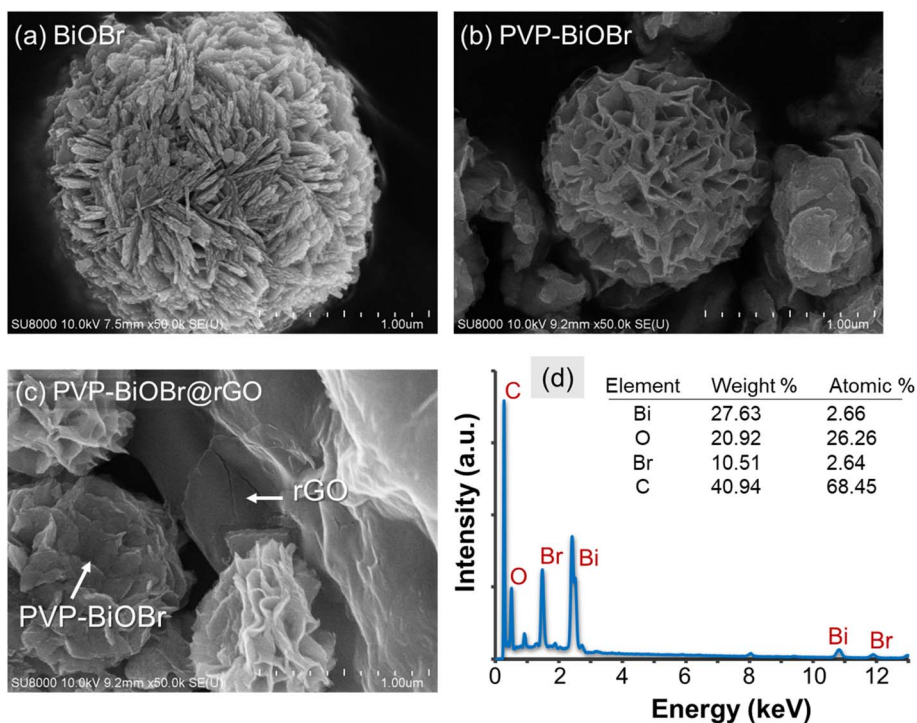

Fig. 3 SEM imagery of (a) bare BiOBr, (b) PVP-BiOBr, (c) PVP-BiOBr@rGO composites, and (d) EDX spectrum of PVP-BiOBr@rGO.

Table 1 Surface area, pore volume, and average pore diameter of various catalysts
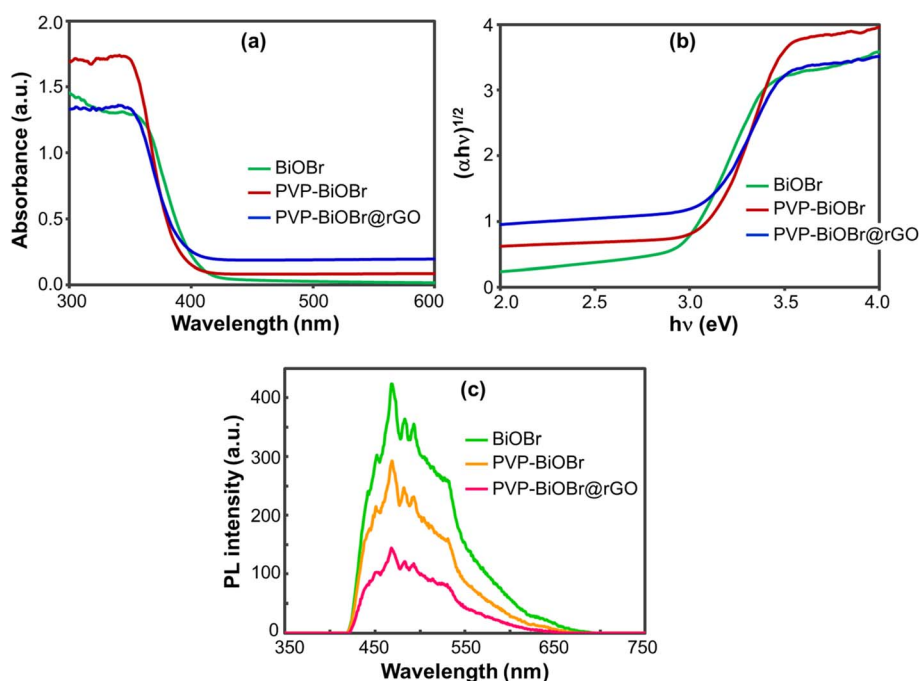
Catalyst	Surface area ($m^2 g^{-1}$)	Pore volume ($cm^3 g^{-1}$)	Average pore diameter (nm)
BiOBr	12.46	0.047	11.62
PVP-BiOBr	25.64	0.085	9.80
PVP-BiOBr@rGO	47.59	0.085	7.58

the composite shows much higher C and O levels due to the added PVP and rGO.[17]

Nitrogen adsorption–desorption isotherms were investigated at 77.3 K to determine the surface area and pore characteristics of the prepared catalysts. According to the IUPAC classification, the BiOBr-PVP@rGO catalyst exhibited a Type IV isotherm with hysteresis (Fig. S3†). Type IV isotherms are given by mesoporous materials, and hysteresis occurs for pore sizes greater than 4 nm.[34] The average pore diameter of PVP-BiOBr@rGO was 7.58 nm in the current study. BET surface area, BJH pore volume, and average pore diameter of three catalysts are compared in Table 1. The surface area of BiOBr is 12.46 $m^2 g^{-1}$, while PVP-BiOBr exhibits a higher value, 25.64 $m^2 g^{-1}$. The surface area becomes greater for PVP-BiOBr@rGO (47.59 $m^2 g^{-1}$) when incorporating rGO into the composite. Our results agree with the literature, as PVP and rGO can increase the surface area when incorporated into hybrid composites.[16,20] Additionally, the PVP-BiOBr@rGO catalyst has a high pore volume. Owing to the large surface area and pore volume, this catalyst enables efficient adsorption with a great number of active sites, benefiting photocatalysis.[24]

Absorption edge and band gap energy are crucial factors for photocatalysis. From the UV-vis diffuse reflectance spectroscopy (DRS) spectra in Fig. 4a, the absorption edge of the prepared catalysts has an approximately 400 nm wavelength, supporting the possibility of visible-light-driven photoactivity. Among the catalysts, PVP-BiOBr@rGO exhibited stronger absorption across the visible range from 400–600 nm. This implies that the catalyst can absorb more visible light photons, facilitating its photoactivity to a greater degree. Tauc plots are presented in Fig. 4b to gain insight into the band gap energy (E_g) of each catalyst. The BiOBr composite is an indirect transition semiconductor.[19,35] Therefore, indirect band gap energy was evaluated from the plot. The E_g values were 2.90, 3.00 and 2.94 eV for BiOBr, PVP-BiOBr and PVP-BiOBr@rGO, respectively. Band gap energy is influenced by the particle size of the catalyst, following quantum confinement.[36,37]

Charge recombination refers to a phenomenon in which photoexcited charges (electrons and holes) coalesce. This results in light emission or photoluminescence (PL). A stronger PL intensity yields a higher rate of recombination, limiting the photocatalytic performance. As shown in Fig. 4c, with a 250 nm excitation wavelength (λ_{ex}), the PL spectra of the three different catalysts give similar maximum emission peaks at a 468 nm (λ_{em}) wavelength. With incorporation of PVP and rGO into the composites, the PL intensity of the PVP-BiOBr@rGO catalyst is greatly diminished, inferring good charge transfer and thus lowering recombination of electron–hole pairs.[20] This reduced PL intensity suggests that incorporation of PVP and rGO effectively enhances charge separation within the PVP-BiOBr@rGO catalyst, ultimately improving its photocatalytic performance.

Fig. 4 (a) UV-vis DRS spectra, (b) Tauc plots for indirect band gap energy calculation, and (c) PL spectra (at λ_{ex} = 250 nm) of BiOBr, PVP–BiOBr and PVP-BiOBr@rGO.
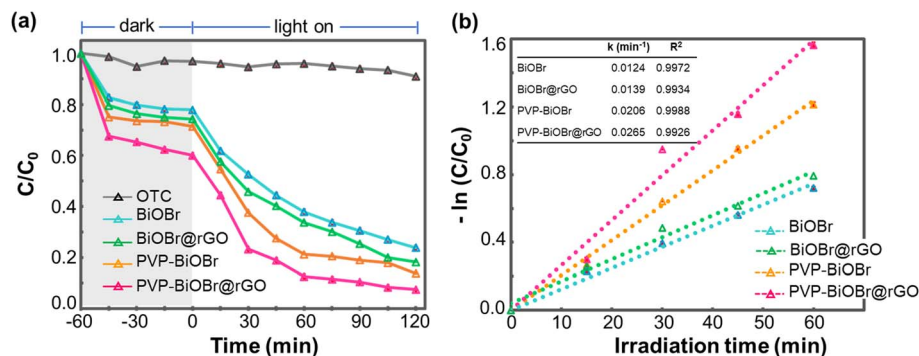
Fig. 5 (a) Decreased OTC concentration in the presence of bare BiOBr, BiOBr@rGO, PVP–BiOBr, and PVP–BiOBr@rGO photocatalysts, and (b) first-order kinetic curves of OTC degradation over the different photocatalysts.

3.2. Optimal conditions for photocatalytic activity (batch experiment)

3.2.1 Type of photocatalyst. The photocatalytic performance of BiOBr, BiOBr@rGO, PVP-BiOBr, and PVP-BiOBr@rGO was evaluated based on photodegradation of OTC under visible light irradiation. Each catalyst was tested under the same conditions. For comparison, a blank test (photolysis of OTC) was done. OTC is negligibly decomposed in the presence of no photocatalyst. The absorption properties of the catalysts were explored under dark conditions. In Fig. 5a, all catalysts attained adsorption–desorption equilibrium within 60 min. PVP-BiOBr@rGO demonstrated a greater adsorption capability, due to its larger surface area and pore volume (Table 1). After achieving adsorption–desorption equilibrium, the photocatalytic activities were monitored under light illumination. Photodegradation of OTC by PVP-BiOBr@rGO approached 92.5% in 120 min, which is greater than that of BiOBr (76.1%), BiOBr@rGO (81.7%), and PVP-BiOBr (86.2%) (Fig. 5a). The photocatalytic performance of PVP-BiOBr@rGO also surpasses that of BiOBr@rGO, substantiating the important role of PVP in the composite. Integration of rGO into PVP-BiOBr promoted photogenerated electron transfer and thus prolong charge carrier separation.[19,22–24] Consequently, the photocatalytic performance of PVP-BiOBr@rGO was drastically improved.

To better understand the reaction kinetics of the OTC degradation catalyzed by the as-prepared photocatalysts, the experimental data were fitted using a first-order model according to eqn (2):[23,38]

$$-\ln\left(\frac{C_t}{C_0}\right) = kt \qquad (2)$$

where k represents the first-order rate constant of OTC photocatalytic degradation and t is the irradiation time. As can be seen in Fig. 5b, PVP-BiOBr@rGO offered the maximum degradation rate constant ($0.0265\ min^{-1}$), whereas the rate constants obtained from BiOBr, BiOBr@rGO, and PVP-BiOBr were $0.0124\ min^{-1}$, 0.0139 and $0.0206\ min^{-1}$, respectively.

3.2.2 Effect of PVP-BiOBr: rGO content. Different mass ratios of PVP-BiOBr and rGO in the composite may affect the photocatalytic activities of PVP-BiOBr@rGO, therefore the impact of this parameter was studied. Composites with mass ratios of PVP-BiOBr (100 mg): rGO (1, 5, 20 and 50 mg) were synthesized, and their photocatalytic performance was compared (Fig. 6a). After 120 min of light illumination, the degradation percentages of OTC were enhanced to about 85.8, 86.8 and 91.9% for composites containing 1, 5 and 20 mg RGO, respectively. However, a higher rGO content (50 mg) gave poorer degradation efficiency, 85.4%. This is presumably due to excessive rGO impeding light from reaching the PVP-BiOBr, thereby decreasing its degradation activity. A similar phenomenon was observed for other photocatalysts containing rGO.[23,39] Based on these results, a suitable content of PVP-BiOBr (100
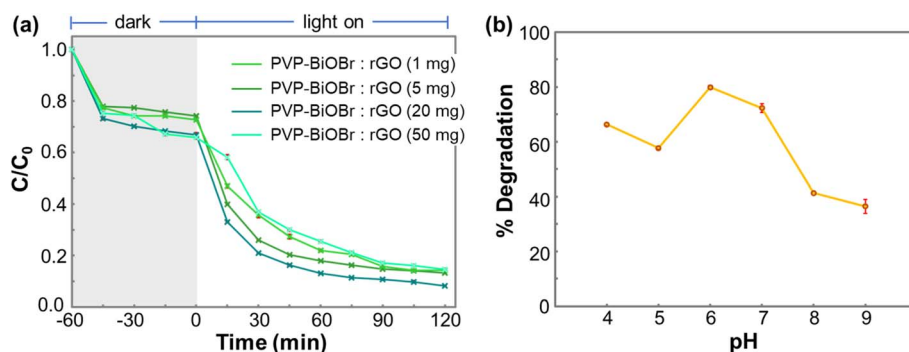

Fig. 6 (a) Effect of mass ratio of PVP–BiOBr (100 mg) and rGO (i.e., 1, 5, 20 and 100 mg) in a PVP–BiOBr@rGO composite, and (b) effect of pH on photocatalytic degradation of OTC.

mg) : rGO (20 mg), was chosen as a photocatalyst for degrading OTC.

3.2.3 Effect of pH. pH can influence both the chemical structure of organic pollutants and the surface charge of photocatalysts,[38] so the effect of pH on OTC degradation by PVP-BiOBr@rGO was investigated. OTC solutions with pH values ranging from 4 to 9 were prepared by adjustment with 0.1 M HCl or NaOH, as appropriate. As shown in Fig. 6b, the optimal degradation of OTC by a PVP-BiOBr@rGO composite occurred in the pH range of 6 to 7. OTC has three pK_a values, 3.22, 7.68, and 8.94.[40] In this pH range, the dominant OTC species is a zwitterion.[41] The point of zero charge (pH_{pzc}), which refers to the pH at which the net charge on the particle surface is zero, was also studied. The pH_{pzc} of PVP-BiOBr@rGO was 6.2 (Fig. S5†), consistent with an earlier study.[42] At pH 6–7, the catalyst surface charge is nearly neutral, making it favorable for the adsorption of zwitterionic OTC molecules. Therefore, in this study, the pH of the wastewater sample was adjusted to 6–7 before treatment. These results highlight the importance of optimizing the pH conditions for photocatalytic reactions, where pH control could be a key factor in maximizing photocatalytic efficiency.

3.3. Photodegradation mechanism

To identify the main reactive species involved in OTC removal, radical trapping experiments were conducted.[43,44] Isopropanol (IPA), 1,4-benzoquinone (BQ), and ethylenediaminetetraacetic acid (EDTA) were used as scavengers for hydroxyl radicals (OH•), superoxide anion radicals (O_2•−), and photogenerated holes (h+), respectively. These scavengers were individually added to the OTC solution prior to the introduction of the PVP-BiOBr@rGO photocatalyst. Experimental details are provided in the ESI.†

The effects of different scavengers on OTC degradation are shown in Fig. 7a. Notably, the photocatalytic efficiency dropped significantly to approximately 20% upon the addition of BQ (Fig. 7b), highlighting the dominant role of superoxide anion radicals in the degradation process. Hydroxyl radicals and photogenerated holes were found to play subordinate roles. As illustrated in Fig. 7c, the rate constant (k) in the presence of BQ was 0.0016 min^{-1}, compared to 0.0073 min^{-1} with no scavenger. This ~4.6-fold reduction in the degradation rate further confirms the substantial role of O_2•− in the OTC degradation mechanism.

Furthermore, a terephthalic acid (TA) probe experiment was conducted to show that there are hydroxyl radicals generated by PVP-BiOBr@rGO during the photocatalytic process. In principle, TA reacts with hydroxyl radical to form a fluorescent product, 2-hydroxyterephthalic acid (HTA) (mechanism in Fig. S4†). After dispersing PVP-BiOBr@rGO into the TA solution, the suspension was then exposed to light. At a 315 nm excitation wavelength, the PL intensity of the HTA product was then monitored (Fig. 7d). The PL intensity increased over time, verifying gradual photogeneration of hydroxyl radicals.[45] These results confirm that the PVP-BiOBr@rGO catalyst effectively generates reactive radicals under light exposure, supporting its potential for enhanced photocatalytic activity.

3.4. Flow-circulation system for degradation of OTC in wastewater

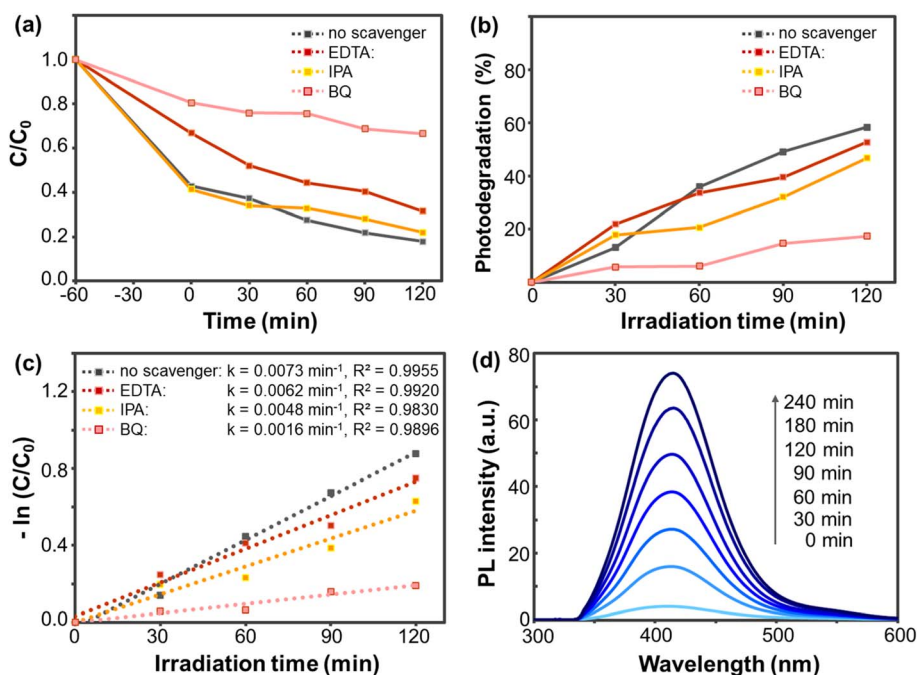In this study, a flow-circulation system was designed to demonstrate the photocatalytic performance of a PVP-

Fig. 7 (a) Decrease in C/C_0 during photodegradation, (b) photodegradation efficiencies, (c) the rate constants (k) for OTC degradation in the presence of various scavengers, and (d) hydroxyl radical trapping PL spectral changes at different times over PVP-BiOBr@rGO in a terephthalic acid solution (λ_{ex} = 315 nm).
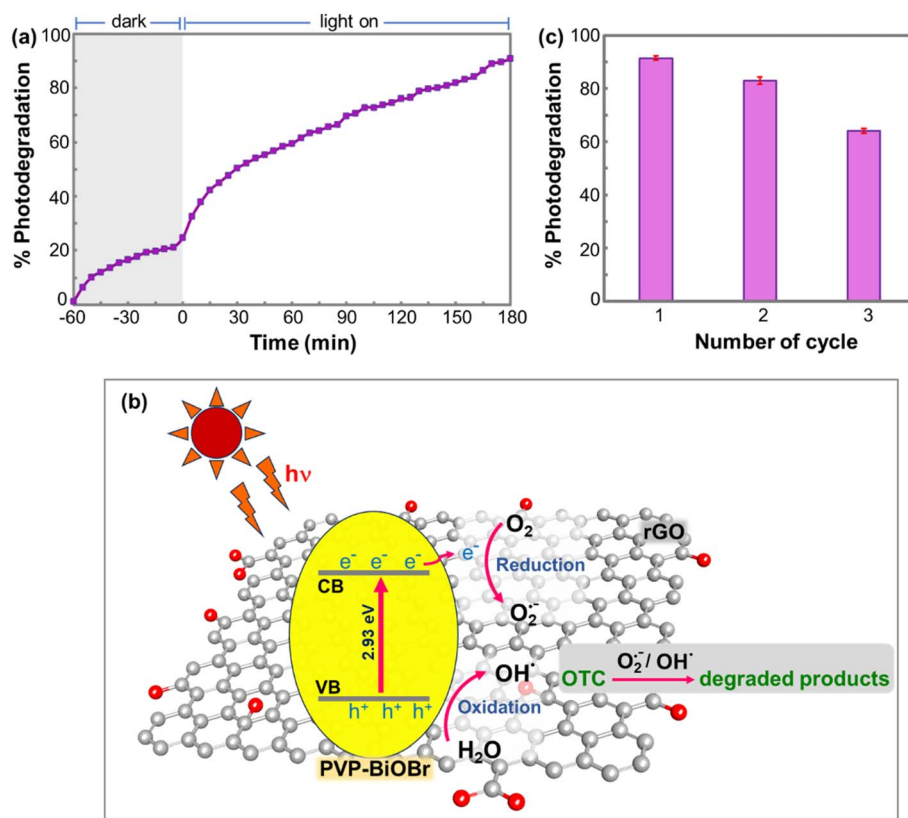
Fig. 8 (a) Photodegradation of OTC under a flow-circulation system (conditions: flowrate 1.0 mL min^{-1}, 10 mg of PVP-BiOBr@rGO in the catalyst column, 40 mL of 10 mg L^{-1} OTC, solution pH = 6), (b) a schematic illustration of the photocatalytic process of PVP-BiOBr@rGO for OTC degradation, and (c) PVP-BiOBr@rGO column performance over three cycles.

BiOBr@rGO composite for real-world degradation of oxytetracycline (OTC) in fish farm wastewater. The flow system was set up as presented in Fig. 1. Before irradiation, the wastewater sample flowed through the system in the dark for 60 min before illumination. The OTC concentration in the sample was monitored in-line every 5 min using a spectrophotometer. OTC photodegradation using the flow-circulation system employing a PVP-BiOBr@rGO composite is depicted in Fig. 8a. Photodegradation efficiency reached 90.3% within 180 min. The flow system has shown several advantages for photocatalytic/adsorptive applications.[27,28] These include (i) the photocatalyst was packed inside a column and did not contaminate the water sample, (ii) the flow system runs in an automated and continuous mode which provides for convenient operation, and (iii) this system establishes simultaneous degradation and detection, which is important for real-world water treatment. An overview of the photodegradation mechanism of OTC by the PVP-BiOBr@rGO photocatalyst is illustrated in Fig. 8b. With light radiation, electrons are excited from the valence bands (VB) to the conduction bands (CB) of the PVP-BiOBr. Subsequently, the electrons in the conduction band are transferred to rGO, which separates the electrons from holes in the valence bands. The photogenerated electrons and holes can produce reactive radical species that effectively decompose OTC contaminants in water samples.

The reusability of the PVP-BiOBr@rGO catalyst column was tested. After the first use, the column was regenerated by flushing it with water before a subsequent cycle. The OTC degradation at the first cycle was 90.3% which decreased to 83.0% and 63.4% after the second and third cycles, respectively (Fig. 8c). Accordingly, it is recommended the catalyst column can be used for two cycles, with an efficiency of up to 80%. The decline in photocatalytic efficiency observed in the reused column was investigated by examining the structure and morphology of the PVP-BiOBr@rGO catalyst before and after use. XRD patterns of both fresh and used samples showed no significant differences, and SEM images confirmed that the overall morphology remained largely unchanged (Fig. S6†). These results indicate good structural and morphological stability of the PVP-BiOBr@rGO catalyst. However, during the recycling process, some catalyst particles were found to accumulate and obstruct the membrane at the column outlet. This blockage likely limited the exposure of active sites and hindered light penetration into the aggregated catalyst, thereby contributing to the reduced photocatalytic performance in the reused column.[46]

The photocatalytic performance of various photocatalysts for the degradation of OTC has been widely studied. A summary of the photocatalytic efficiency of our PVP-BiOBr@rGO composite, alongside previously reported results, is presented in Table 2.

RSC Advances

Table 2 Comparison of OTC degradation using different photocatalysts

Catalyst	Studied system	Light source	OTC conc.	Catalyst dosage	% degradation	Time (min)	Ref.
ZnO	Batch	UV-A	$10 mg L^{-1}$	$1 g L^{-1}$	42.1	25	7
g-C$_3$N$_4$	Batch	Visible	$10 mg L^{-1}$	50 mg	33.9	50	8
ZnO/NiO	Batch	Visible	$40 mg L^{-1}$	200 mg	79.0	120	9
CuO/Bi$_2$WO$_6$	Batch	Visible	$50 mg L^{-1}$	$0.8 g L^{-1}$	86.3	180	10
BiOBr/rGO	Batch	Visible	$5 mg L^{-1a}$	50 mg	73.0	120	47
KB/BMO-GO	Batch	Visible	$50 mg L^{-1}$	20 mg	93.3	90	11
AgI/BiOBr/RGO	Batch	Visible	$20 mg L^{-1a}$	50 mg	94.2	80	20
g-C$_3$N$_4$/BiOCl/CdS	Batch	Visible	$10 mg L^{-1}$	50 mg	87.0	240	33
PVP-BiOBr@rGO	Flow	Visible	$10 mg L^{-1}$	10 mg	90.3	180	This work

^{a} As a tetracycline (TC) concentration.

Single-component catalysts typically exhibit limited activity for OTC removal, achieving efficiencies of only 33.9% to 42.1%.[7,8] In contrast, binary composites show enhanced performance, with efficiencies ranging from 79% to 86%.[9,10,47] Notably, ternary composites demonstrate even greater photocatalytic activity, with reported efficiencies reaching 87% to 94.2%.[11,20,33] These findings underscore the superior advantages of ternary heterostructures, which hold strong potential for efficient OTC degradation.

4. Conclusions

This work successfully developed a new photocatalytic flow-circulation system using PVP-BiOBr for OTC removal from wastewater. By combining PVP-BiOBr with rGO, the composite exhibited efficient photocatalytic performance toward OTC degradation. PVP could regulate the structure and morphology of BiOBr, achieving a porous flower-like assembly with a high active surface area. rGO afforded charge carrier transfer and separation, and its adsorption capability also provided a synergistic effect on OTC removal. These factors are key to maximizing the photocatalytic activity of this material. A notable aspect of this work is the system's dual functionality, featuring simultaneous OTC detection and degradation in a continuous flow. During circulation, automated degradation and real-time monitoring are accomplished. This system is scalable and applicable to real-world water treatment. Furthermore, in the current work, the developed flow system demonstrated OTC elimination from fish farm wastewater. Our results confirmed that the system performance yielded ≥ 90% OTC degradation, and the photocatalyst column could be used two times. This photocatalytic flow-circulation system holds promise for water purification, especially in agricultural and aquaculture wastewater treatment where antibiotic contamination is a concern. The system provides a sustainable solution for industrial wastewater management.

Data availability

The data supporting this article have been included as part of the ESI.†

Author contributions

Saowapak Teerasong: conceptualization, methodology, data curation, writing – original draft, funding acquisition, supervision. Nichakarn Suknakhin: methodology, investigation. Thanamat Sonsaket: methodology, investigation. Wanatchaporn Teerasong: methodology, investigation. Chesta Ruttanapun: writing – review & editing. Chaval Sriwong: writing – review & editing. Apiwat Chompoosor: data curation, writing – review & editing. Suwat Nanan: methodology, writing – review & editing.

Conflicts of interest

There are no conflicts to declare.

Acknowledgements

References

1 M. J. Martin, S. E. Thottathil and T. B. Newman, *Am. J. Public Health*, 2015, **105**, 2409.

2 S. Reardon, *Nature*, 2023, **614**, 397.

3 L. Xu, H. Zhang, P. Xiong, Q. Zhu, C. Liao and G. Jiang, *Sci. Total Environ.*, 2021, **753**, 141975.

4 R. Daghrir and P. Drogui, *Environ. Chem. Lett.*, 2013, **11**, 209.

5 S.-Z. Li, X.-Y. Li and D.-Z. Wang, *Sep. Purif. Technol.*, 2004, **34**, 109.

6 T. Hu, H. Lv, S. Shan, Q. Jia, H. Su, N. Tian and S. He, *RSC Adv.*, 2016, **6**, 73741.

7 S. Yildiz, G. T. Canbaz and H. Mihçiokur, *Environ. Prog. Sustainable Energy*, 2024, **43**, e14384.

8 H. Ding, Z. Liu, Q. Zhang, X. He, Q. Feng, D. Wang and D. Ma, *RSC Adv.*, 2022, **12**, 1840.

9 R. Mou, Z. Liu, D. Zhang and A. Yang, *Chem. Phys. Lett.*, 2023, **829**, 140741.

10 X. Shi, B. Liu, G. Meng, P. Wu, J. Lian, W. Kong and R. Liu, *J. Alloys Compd.*, 2024, **1002**, 175219.

11 Y. Zhang, M. Wang, D. Chen, N. Li, Q. Xu, H. Li and J. Lu, *J. Colloid Interface Sci.*, 2024, **668**, 437.

12 Y. Zhu, Y. Liu, Q. Ai, G. Gao, L. Yuan, Q. Fang, X. Tian, X. Zhang, E. Egap, P. M. Ajayan and J. Lou, *ACS Mater. Lett.*, 2022, **4**, 464.

13 Y. Yang, Z. Chen, H. Huang, Y. Liu, J. Zou, S. Shen, J. Yan, J. Zhang, Z. Zhuang, Z. Luo, C. Yang, Y. Yu and Z. Zou, *Appl. Catal., B*, 2023, **323**, 122146.

14 G.-Q. Zhao, J. Hu, J. Zou, X. Long and F.-P. Jiao, *J. Environ. Chem. Eng.*, 2022, **10**, 107226.

15 S. S. Imam, R. Adnan and N. H. Mohd Kaus, *J. Environ. Chem. Eng.*, 2021, **9**, 105404.

16 T. Senasu, T. Chankhanittha, K. Hemavibool and S. Nanan, *Catal. Today*, 2022, **384–386**, 209.

17 B. Zhang, M. Zhang, L. Zhang, P. A. Bingham, W. Li and S. Kubuki, *Appl. Surf. Sci.*, 2020, **530**, 147233.

18 Y. Li, Z. Wang, B. Huang, Y. Dai, X. Zhang and X. Qin, *Appl. Surf. Sci.*, 2015, **347**, 258.

19 W. Tie, S. S. Bhattacharyya, C. Han, S. Qiu, W. He and S. H. Lee, *ACS Omega*, 2022, 7, 35805.

20 J. Chen, X. Xiao, Y. Wang, M. Lu and X. Zeng, *J. Alloys Compd.*, 2019, **800**, 88.

21 Z. Yang, F. Cheng, X. Dong and F. Cui, *RSC Adv.*, 2015, **5**, 68151.

22 A. Mondal, A. Prabhakaran, S. Gupta and V. R. Subramanian, *ACS Omega*, 2021, **6**, 8734.

23 B. Chai, J. Li and Q. Xu, *Ind. Eng. Chem. Res.*, 2014, **53**, 8744.

24 N. Clament Sagaya Selvam, Y. G. Kim, D. J. Kim, W.-H. Hong, W. Kim, S. H. Park and W.-K. Jo, *Sci. Total Environ.*, 2018, **635**, 741.

25 M. Xu, Y. Wang, E. Ha, H. Zhang and C. Li, *Chemosphere*, 2021, **265**, 129013.

26 Z. Du, F. Liu, G. Ding, Y. Dan and L. Jiang, *Mater. Chem. Phys.*, 2021, **262**, 124239.

27 H. Mandor, E.-S. Z. El-Ashtoukhy, O. Abdelwahab, N. K. Amin and D. A. Kamel, *Alexandria Eng. J.*, 2022, **61**, 3385.

28 S. Teerasong, T. Saenghirun, T. Sunthornchainukul, S. Thammaso, A. Chompoosor and S. Nanan, *ACS Omega*, 2024, **9**, 29644.

29 C. Phrompet, K. Maneesai, W. Tuichai, A. Karaphun, C. Sriwong and C. Ruttanapun, *J. Energy Storage*, 2020, **30**, 101474.

30 S. Abbas, S. Manzoor, M. Abdullah, K. H. Mahmoud, A. G. Abid, M. S. Khan, G. Yasmeen, A. S. A. Alsubaie, S. Manzoor and M. N. Ashiq, *J. Mater. Sci.: Mater. Electron.*, 2022, **33**, 25355.

31 Y.-L. Chen, Z.-A. Hu, Y.-Q. Chang, H.-W. Wang, Z.-Y. Zhang, Y.-Y. Yang and H.-Y. Wu, *J. Phys. Chem. C*, 2011, **115**, 2563.

32 D. R. Baganizi, E. Nyairo, S. A. Duncan, S. R. Singh and V. A. Dennis, *Nanomaterials*, 2017, **7**, 165.

33 T. Senasu, N. Lorwanishpaisarn, K. Hemavibool, S. Nijpanich, N. Chanlek and S. Nanan, *Sep. Purif. Technol.*, 2023, **306**, 122735.

34 M. Thommes, K. Kaneko, A. V. Neimark, J. P. Olivier, F. Rodriguez-Reinoso, J. Rouquerol and K. S. W. Sing, *Pure Appl. Chem.*, 2015, **87**, 1051.

35 Y. Wu, H. Ji, Q. Liu, Z. Sun, P. Li, P. Ding, M. Guo, X. Yi, W. Xu, C.-C. Wang, S. Gao, W. Liu and S. Chen, *J. Hazard. Mater.*, 2022, **424**, 127563.

36 M. Khatun, P. Mitra and S. Mukherjee, *Hybrid Adv.*, 2023, **4**, 100079.

37 M. El-Hagary, E. R. Shaaban, S. H. Moustafa and G. M. A. Gad, *Solid State Sci.*, 2019, **91**, 15.

38 S. H. Alwan, K. H. Salem and H. A. Alshamsi, *Mater. Today Commun.*, 2022, **33**, 104558.

39 X. An, K. Li and J. Tang, *ChemSusChem*, 2014, **7**, 1086.

40 Y. Li, H. Wang, X. Liu, G. Zhao and Y. Sun, *Environ. Sci. Pollut. Res.*, 2016, **23**, 13822.

41 J. Lyu, Z. Hu, Z. Li and M. Ge, *J. Phys. Chem. Solids*, 2019, **129**, 61.

42 S. Nethaji, G. Tamilarasan, P. Neehar and A. Sivasamy, *J. Environ. Chem. Eng.*, 2018, **6**, 3735.

43 C. Yu, H. He, X. Liu, J. Zeng and Z. Liu, *Chin. J. Catal.*, 2019, **40**, 1212.

44 H. He, Z. Luo and C. Yu, *Colloids Surf., A*, 2021, **613**, 126099.

45 T. Charbouillot, M. Brigante, G. Mailhot, P. R. Maddigapu, C. Minero and D. Vione, *J. Photochem. Photobiol., A*, 2011, **222**, 70.

46 F. Pellegrino, L. Pellutiè, F. Sordello, C. Minero, E. Ortel, V.-D. Hodoroaba and V. Maurino, *Appl. Catal., B*, 2017, **216**, 80.

47 M. Shkir, S. H. Aldirham, S. AlFaify and A. M. Ali, *Chemosphere*, 2024, **357**, 141934.